IMA Journal of Applied Mathematics (2022) **87**, 291–313
https://doi.org/10.1093/imamat/hxac006
Advance Access publication on 3 April 2022

Quasisteady models for weld temperatures in fused filament fabrication

D. A. Edwards*
Department of Mathematical Sciences, University of Delaware, Newark, DE 19716, USA
*Corresponding author: dedwards@udel.edu

[Received on 18 August 2021; revised on 4 February 2022; accepted on 20 February 2022]

During fused filament fabrication (FFF), strands of hot extruded polymer are layered onto a cooler substrate. The bond strength between layers is related to the weld temperature at the polymer/substrate interface, and hence understanding temperature evolution is of keen interest. A series of increasingly sophisticated models is presented: a standard heat equation, an unsteady fin equation and a fin equation with a heat-loss jump condition. Each is analytically tractable and uses a quasisteady approximation for the temperature in the growing substrate. The jump condition introduces the complication of a non-self-adjoint problem, but fits the experimental data very well.

Keywords: 3-D printing; fused filament fabrication; heat equation; weld temperature; non-self-adjoint problems.

1. Introduction

Additive manufacturing is incredibly popular for various types of production in many industries, such as aerospace (Najmon *et al.*, 2019), consumer devices and gadgets (Gibson *et al.*, 2009), medical and dental devices (Arslan-Yildiz *et al.*, 2016; Noort, 2012) and housing construction (Hager *et al.*, 2016; Wu *et al.*, 2016). In the process called fused filament fabrication (FFF, commonly called 3-D printing), the desired object is composed of extruded polymer layers stacked on top of one another. Not surprisingly, the primary mode of failure for such objects is delamination of the layers. Therefore, in order to guarantee strength of the object as a whole, the individual layers must be securely bonded to one another (Coasey *et al.*, 2020; Davis *et al.*, 2017).

The strength of the bond is related to the *weld temperature*; that is, the temperature at the interface between adjacent layers. The extruded layers have high curvature (Coasey *et al.*, 2020; Seppala & Migler, 2016), so initially the contact area between the new layer and the previously extruded layers (which we shall call the *substrate*) is quite small. However, at a hotter weld temperature, the molecules relax more quickly, creating a bonding region that is more pliable and fluid-like. When combined with processing conditions that press the new layer onto the substrate, this increases the number of entanglements formed across the layer-substrate interface driven by the reconfiguration of molecules: hence the layers fuse together more tightly (Luo *et al.*, 2021; Rashid & Koç, 2021; Sun *et al.*, 2008; Turner *et al.*, 2014; Yang & Pitchumani, 2002).

Much work has been devoted to intricate computer simulations of temperature profiles throughout the substrate (Baeza-Campuzaño & Castano, 2021; Behdani *et al.*, 2020; Costa *et al.*, 2015; D'Amico & Peterson, 2020; Das *et al.*, 2021; Lotero *et al.*, 2017; Mu *et al.*, 2015; Nath *et al.*, 2020; Rashid & Koç, 2021; Xia *et al.*, 2018). Though these efforts provide detailed results, it can be difficult to interpret their dependence on material and experimental parameters, which is key to process optimization. For such purposes, more tractable analytical models can provide useful results (Edwards & Mackay, 2020;

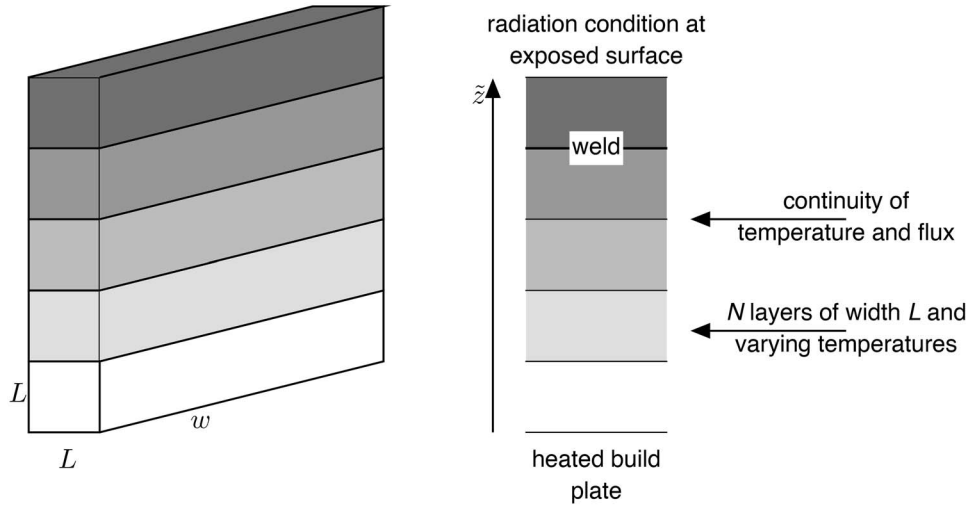

FIG. 1. Schematic of stack. Left: Three-dimensional idealization. Right: One-dimensional model .

positive $\tilde{z}$, and impose the boundary condition

$$\tilde{T}(0,\tilde{t}) = \tilde{T}_{\mathrm{p}}. \tag{2.2}$$

As it exits the hot end, each deposited layer is heated to some temperature $\tilde{T}_{\mathrm{h}}$, where the subscript 'h' refers to 'heater'. The layers are laid down at regular intervals, spaced t_{l} apart, where the subscript 'l' refers to 'layer'. Thus the spatial domain for the problem increases stepwise in time (see Fig. 2).

This discussion motivates the following scalings:

$$t = \frac{\tilde{t}}{t_{\mathrm{l}}}, \qquad z = \frac{\tilde{z}}{L}, \qquad T(z,t) = \frac{\tilde{T}(\tilde{z},\tilde{t}) - \tilde{T}_{\mathrm{p}}}{\Delta T}, \qquad \Delta T = \tilde{T}_{\mathrm{h}} - \tilde{T}_{\mathrm{p}}. \tag{2.3}$$

Substituting (2.3) into (2.1) and (2.2), we obtain

$$\frac{\partial T}{\partial t} = \alpha^2 \frac{\partial^2 T}{\partial z^2}, \qquad \alpha^2 = \frac{k t_{\mathrm{l}}}{\rho c_p L^2} = \frac{\text{printing interval}}{\text{diffusion time}}, \tag{2.4a}$$

$$T(0,t) = 0. \tag{2.4b}$$

Here α^2 is the thermal diffusivity.

If n layers have been applied, then $\tilde{z} = nL$ is the surface where the topmost layer is exposed to the room air. At that surface, a Robin-type radiation condition applies:

$$-k\frac{\partial \tilde{T}}{\partial z}(nL,\tilde{t}) = h[\tilde{T}(nL,\tilde{t}) - \tilde{T}_{\mathrm{e}}],$$

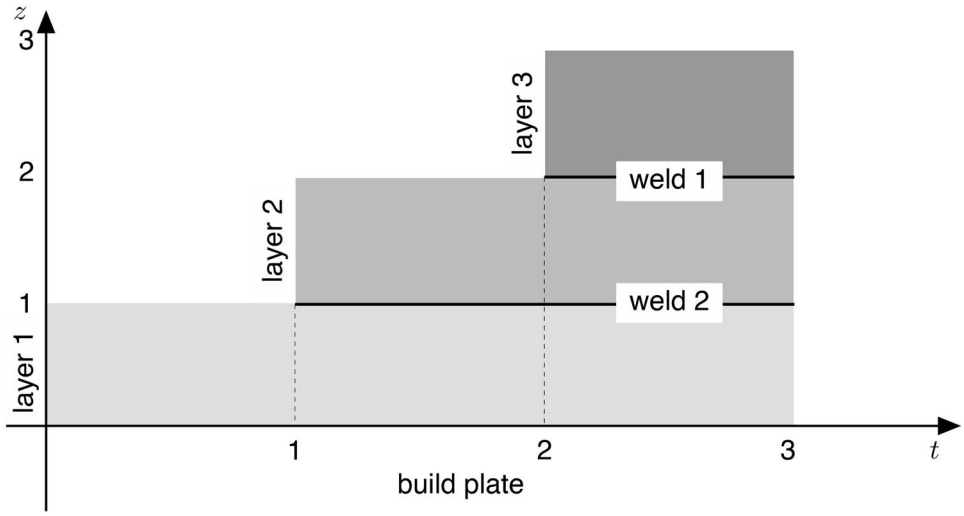

FIG. 2. Sequence of layers as applied (dimensionless).

where h is the heat transfer coefficient and $\tilde{T}_e \leq \tilde{T}_p$ is the external temperature (hence the subscript 'e'). Note the negative sign on the left-hand side to make the signs of the fluxes balance. Substituting (2.3) into the above equation, we have

$$\frac{\partial T}{\partial z}(n,t) = -\nu[T(n,t) - T_e], \quad n-1 < t < n; \qquad \nu = \frac{hL}{k}, \tag{2.5}$$

where we have used the same convention as in (2.3) to remove the tilde from T_e, which is negative. Also note the range of time for which (2.5) holds is limited, ending as the next layer is added.

Similarly, the problem 'resets' after every unit of time, with a new 'initial' condition being imposed as the result of adding the layer. In particular, the nth layer is added at time $t = n-1$ (see Fig. 2). Hence the temperature at that time is given by the previous temperature in the substrate, and the heated value in the added layer:

$$T(z,(n-1)^+) = \begin{cases} T(z,(n-1)^-), & 0 < z \leq (n-1), \\ 1, & n-1 < z \leq n, \end{cases} \tag{2.6}$$

where we have used (2.3) to simplify the second line. (We note that all of our analysis will hold in the case where $n = 1$ and the first line of (2.6) is neglected.)

2.1 *The quasisteady approximation*

In order to understand better the dependence of our solutions on the material and experimental parameters in the problem, we want those solutions to be as analytically tractable as possible. To that end, we introduce the *quasisteady approximation*. To wit, we note from the Appendix that in the experiment we are attempting to match, the layers are laid down around 7 s apart. This gives the temperature in the substrate time to equilibrate before the next layer is laid down.

Therefore, we approximate the temperature of the substrate at time n by its steady state:

$$T(z,(n-1)^{-}) = T(z,\infty) \equiv \sigma_{n-1}(z), \qquad 0 < z < n-1. \tag{2.7}$$

Here the subscript $n-1$ refers to the fact that it is the steady state for $n-1$ layers occupying the region $0 < z < n-1$.

For later purposes, it is more convenient to solve for σ_n; substituting $T(z,t) = \sigma_n(z)$ into (2.4a) and (2.5), we have

$$\frac{\mathrm{d}^2\sigma_n}{\mathrm{d}z^2} = 0,$$

$$\sigma_n(0) = 0, \tag{2.8a}$$

$$\frac{\mathrm{d}\sigma_n}{\mathrm{d}z}(n) = -\nu[\sigma_n(n) - T_\mathrm{e}], \tag{2.8b}$$

the solution of which is

$$\sigma_n(z) = \frac{\nu T_\mathrm{e} z}{1+n\nu}.$$

2.2 *The Fourier solution*

Given that the problem 'resets' with a new initial condition every time a new layer is applied, it is convenient to introduce the new variable

$$\tau = t - (n-1). \tag{2.9}$$

(Technically, we should call the variable τ_n, but for simplicity of interpretation, we suppress the subscript n unless necessary.) Moreover, since we have solved for the steady-state solution separately, we introduce the new variable ψ, which tracks the transients:

$$T(z,t) = \sigma_n(z) + \psi(z,\tau). \tag{2.10}$$

Substituting (2.10) into (2.4a) and (2.5) yields the following:

$$\frac{\partial\psi}{\partial\tau} = \alpha^2\frac{\partial^2\psi}{\partial z^2}, \qquad 0 \le z \le n, \quad \tau > 0, \tag{2.11}$$

$$\psi(0,\tau) = 0, \qquad \frac{\partial\psi}{\partial z}(n,\tau) = -\nu\psi(n,\tau). \tag{2.12}$$

The system for ψ is homogeneous; letting $\psi(z,\tau) = F(\tau)u(z)$, we obtain

$$F' + \alpha^2\lambda^2 F = 0 \qquad \Longrightarrow \qquad F = \exp\left(-\alpha^2\lambda^2\tau\right), \tag{2.13}$$

where the eigenvalues λ are determined by the system

$$u'' + \lambda^2 u = 0, \tag{2.14}$$

$$u(0) = 0, \tag{2.15a}$$

$$u'(n) = -\nu u(n). \tag{2.15b}$$

Solving (2.14) subject to (2.15a) yields

$$u(z) = \sin\lambda z, \qquad \tan\lambda n = -\frac{\lambda}{\nu}, \tag{2.16}$$

which has an infinite number of positive solutions, as required.

Then using the standard separation-of-variables form, we have

$$\psi(z,\tau) = \sum_{m=1}^{\infty} c_m \exp\left(-\alpha^2\lambda_m^2\tau\right)\sin\lambda_m z, \tag{2.17}$$

$$c_m = \frac{1}{||u_m||^2}\int_0^n \psi(z,0)\sin\lambda_m z\,\mathrm{d}z, \tag{2.18a}$$

$$||u_m||^2 = \int_0^n \sin^2\lambda_m z\,\mathrm{d}z = \frac{1}{2}\left(n + \frac{\cos^2\lambda_m n}{\nu}\right). \tag{2.18b}$$

Substituting (2.7) and (2.10) into (2.6), we obtain

$$\psi(z,0) = \begin{cases} \sigma_{n-1}(z) - \sigma_n(z), & 0 < z \le n-1, \\ 1 - \sigma_n(z), & n-1 < z \le n. \end{cases} \tag{2.19}$$

Then computing the c_m, we have

$$||u_m||^2 c_m = H(n-1) - H(n), \qquad H(y) = \frac{\nu T_e}{1+y\nu}\int_0^y z\sin\lambda_m z\,\mathrm{d}z + \frac{\cos\lambda_m y}{\lambda_m}, \tag{2.20}$$

$$H(n) = \frac{(1-T_e)\cos\lambda_m n}{\lambda_m}, \tag{2.21a}$$

$$H(n-1) = \frac{\nu T_e \sin\lambda_m(n-1)}{\lambda_m^2[1+(n-1)\nu]} + \frac{[1+\nu(1-T_e)(n-1)]\cos\lambda_m(n-1)}{\lambda_m[1+(n-1)\nu]}. \tag{2.21b}$$

It can be shown that (2.20) holds even in the case where $n = 1$.

2.3 *Data fitting*

To validate our model, we compare to experimental data from Seppala *et al.* (2017). In keeping with the notation used in that paper, let W_1 be the temperature of the topmost weld ($z = n - 1$) and W_2 be the temperature of the next weld ($z = n - 2$; see Fig. 2). In an experiment, the weld temperature cannot be measured directly; instead, it is inferred as the average of the midpoint temperatures of the layers above and below. Therefore, the weld temperatures are given by

$$W_1(\tau) = \frac{T(n - 1/2, \tau) + T(n - 3/2, \tau)}{2}, \tag{2.22a}$$

$$W_2(\tau) = \frac{T(n - 3/2, \tau) + T(n - 5/2, \tau)}{2}, \quad n > 2. \tag{2.22b}$$

Substituting (2.10) and (2.17) into (2.22a), we have

$$W_1(\tau) = \sigma_n(n - 1) + \sum_{m=1}^{\infty} c_m \exp\left(-\alpha^2 \lambda_m^2 \tau\right) \sin \lambda_m (n - 1) \cos \frac{\lambda_m}{2}. \tag{2.23a}$$

Here the first term simplifies because $\sigma_n(z)$ is linear, while the summands simplify due to a trigonometric identity. Similarly, (2.22b) becomes

$$W_2(\tau) = \sigma_n(n - 2) + \sum_{m=1}^{\infty} c_m \exp\left(-\alpha^2 \lambda_m^2 \tau\right) \sin \lambda_m (n - 2) \cos \frac{\lambda_m}{2}, \quad n > 2. \tag{2.23b}$$

The experimental data we fit come from Seppala *et al.* (2017), Fig. 2a, with $n = 9$ and adjustments as discussed in the Appendix. For all the data fitting, we used 15 modes of the Fourier solution and the `lsqcurvefit` function in Matlab. Moreover, since the convergence of the Fourier series slows noticeably for smaller values of τ, we fit only those data points with $\tau > 0.02$.

A data fit for two welds is shown in Fig. 3. In this simulation, ν is fit and α is chosen to be the lower bound in Table A2. Note that in contrast to the experimental data, there is a wide gap in the solution between the first and second weld temperatures. Hence we conclude that this model, though it may seem to fit the data for a single weld (Coasey *et al.*, 2020), is not sophisticated enough to model multiple weld temperatures. (We present it nevertheless because much of the mathematical work will be used in the more refined models to follow.)

3. The unsteady fin equation

In the model (2.4a), the only mechanism for heat loss is at the exposed end $z = n$. This then leads to a build-up of heat in lower levels of the substrate, which causes the behaviour seen in Fig. 3. In particular, the weld temperature lower in the stack is higher than the weld temperature involving the top layer.

But recall that in the real experiment, the layers form a stack which is exposed to room air not only at $x = n$, but all along the sides (see left of Fig. 1). In order to model this additional heat loss, we may

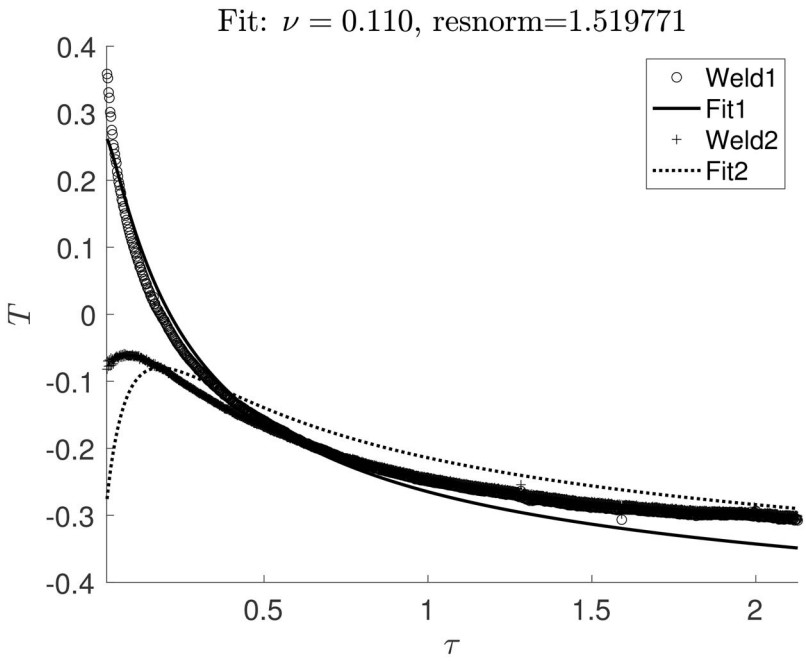

FIG. 3. Plot of two-weld, one-parameter fit of (2.23a) to data in Seppala *et al.* (2017) with $n = 9$. Here α is fixed at the lower bound in Table A2.

use a fin-equation model (Bird *et al.*, 1960, §9.7):

$$\rho c_p \frac{\partial \tilde{T}}{\partial \tilde{t}} = k \frac{\partial^2 \tilde{T}}{\partial \tilde{z}^2} - \frac{P}{A} h(\tilde{T} - \tilde{T}_e),$$

where P is the perimeter and A the area of the fin cross section *orthogonal to the* $\tilde{z}$*-axis*. Bellehumeur *et al.* (2004) use a travelling-wave frame to reduce the PDE to the steady version. However, as we want to track the temperature variations as each layer is applied, we solve the full unsteady version.

Therefore, if we assume that each layer has a square cross-section *as it exits the extruder* (see left of Fig. 1), then $P = 2L + 2w$, $A = Lw$, and we have

$$\rho c_p \frac{\partial \tilde{T}}{\partial \tilde{t}} = k \frac{\partial^2 \tilde{T}}{\partial \tilde{z}^2} - \frac{2L + 2w}{Lw} h(\tilde{T} - \tilde{T}_e). \tag{3.1}$$

We again remark that the true cross section of the extruded polymer is circular; however, it is common to approximate the cross section as a square for computational simplicity (Nath *et al.*, 2020).

The one-dimensional model is obtained by taking $w \to \infty$. Using the scalings from before in that limit, we obtain

$$\frac{\partial T}{\partial t} = \alpha^2 \frac{\partial^2 T}{\partial z^2} - 2\alpha^2 \nu (T - T_e), \tag{3.2}$$

where we have used the parameter definitions in (2.4a) and (2.5). We note that a typical 3-D printed object may consist of several layers applied side-by-side (Bellehumeur *et al.*, 2004; Costa *et al.*, 2015), limiting heat loss to just one side. This would then change the coefficient 2 in the last term of (3.2) to 1.

3.1 *Computing the solution*

All of the other boundary and initial conditions remain the same, so we again look for a steady state, replacing (2.10) with

$$T(z,t) = s(z) + \mathrm{e}^{-2\alpha^2\nu t}\psi(z,t), \tag{3.3}$$

where the form of the second term is motivated by the new sink term. Substituting (3.3) into the fin equation (3.2), we have

$$\alpha^2\frac{\mathrm{d}^2 s}{\mathrm{d}z^2} - 2\alpha^2\nu(s - T_\mathrm{e}) = 0, \tag{3.4}$$

which holds subject to (2.8). Solving (3.4) subject to (2.8a), we obtain

$$s_n(z) = T_\mathrm{e}\left[1 - \frac{\cosh(\sqrt{2\nu}(n-z)+\theta)}{\cosh(n\sqrt{2\nu}+\theta)}\right], \tag{3.5}$$

where θ is a constant obtained by substituting (3.5) into the remaining boundary condition (2.8b):

$$\tanh\theta = \sqrt{\frac{\nu}{2}}. \tag{3.6}$$

Equation (3.6) has a real positive solution for $\nu < 2$, which is consistent with the parameters in the Appendix.

Now substituting (3.3) into (3.2), we obtain the following:

$$\frac{\partial\psi}{\partial t} = \alpha^2\frac{\partial^2\psi}{\partial z^2},$$

which is exactly (2.11). Similarly, since (3.5) satisfies the boundary conditions in (2.8), the conditions in (2.12) also hold. So (2.17) holds.

In (2.19), we must replace σ by s:

$$u(z,0) = \begin{cases} s_{n-1}(z) - s_n(z), & 0 < z \le n-1, \\ 1 - s_n(z), & n-1 < z \le n. \end{cases}$$

Then computing the c_m, we have

$$||u_m||^2 c_m = \int_0^{n-1}[s_{n-1}(z) - s_n(z)]\sin\lambda_m z\,\mathrm{d}z + \int_{n-1}^{n}[1 - s_n(z)]\sin\lambda_m z\,\mathrm{d}z \tag{3.7a}$$

$$= T_e[K(n) - K(n-1)] + \frac{(1-T_e)[\cos\lambda_m(n-1) - \cos\lambda_m n]}{\lambda_m}, \tag{3.7b}$$

$$K(y) = \frac{1}{\cosh(\sqrt{2\nu}y + \theta)} \int_0^y \cosh(\sqrt{2\nu}(y-z) + \theta) \sin\lambda_m z \, dz. \tag{3.8}$$

Computing the K terms, we find the following:

$$K(n) - K(n-1) = \frac{(\nu \sin\lambda_m(n-1) + \lambda_m \cos\lambda_m(n-1))\cosh\theta}{(2\nu + \lambda_m^2)\cosh(\sqrt{2\nu}(n-1) + \theta)}. \tag{3.9}$$

3.2 *Data fitting*

Next we consider the weld temperature. Given that the steady state is no longer linear, the s_n terms must retain their arguments, while the sum term simplifies as before. Thus we have

$$W_1(\tau) = \frac{s_n(n-1/2) + s_n(n-3/2)}{2} + e^{-2\alpha^2\nu t} \sum_{m=1}^{\infty} c_m \exp\left(-\alpha^2\lambda_m^2\tau\right) \sin\lambda_m(n-1) \cos\frac{\lambda_m}{2}, \tag{3.10a}$$

$$W_2(\tau) = \frac{s_n(n-3/2) + s_n(n-5/2)}{2} + e^{-2\alpha^2\nu t} \sum_{m=1}^{\infty} c_m \exp\left(-\alpha^2\lambda_m^2\tau\right) \sin\lambda_m(n-2) \cos\frac{\lambda_m}{2}. \tag{3.10b}$$

We compare the solutions with experimental data in Fig. 4. In this case, we fit both ν and α. Note that with this model, the two weld temperatures converge to nearly the same temperature, as expected. The fit heat transfer coefficient is much smaller in Fig. 4 than in Fig. 3. This is also expected, since in the previous model heat could escape only through the exposed surface $z = n$, which forced the heat transfer coefficient larger to accommodate the heat loss. In the fin model, with heat being lost along the entire height of the stack, the heat transfer coefficient is much lower, and is consistent with the values in the Appendix.

4. Leakage at the first weld

The remaining deficiency in the fit is the overshoot in the second weld temperature for small time. In other words, the fin model overstimates the heat flowing from the applied layer to the substrate.

The reason for this as follows. In contrast to the left of Fig. 5, the layer does not come out of the extruder in a square shape, though it is often modelled that way (Nath *et al.*, 2020). Rather, it comes out in a circular shape which is then pressed into the substrate below, deforming both parts (Coogan & Kazmer (2020); Luo *et al.* (2021); see right of Fig. 5). Thus, only a portion of the width of the layer is in contract with the substrate, which reduces the heat transfer.

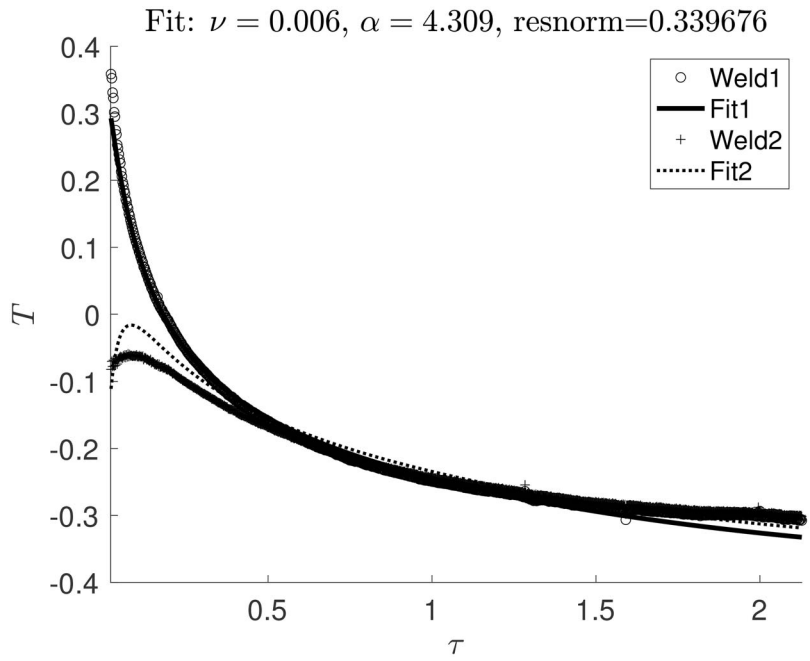

FIG. 4. Plot of two-weld, two-parameter fit of (3.10). Here α is fit as well.

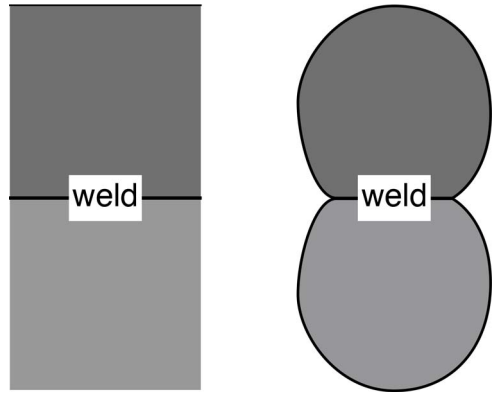

FIG. 5. Schematic of weld structure. Left: first idealization. Right: second idealization.

This contact can be modelled by changing the assumed shape of the layer (Bellehumeur *et al.*, 2004; Gilmer *et al.*, 2019). However, we prefer to retain the assumed square shape while imposing an additional boundary condition on the solution at $z = n - 1$:

$$\frac{\partial T}{\partial x}((n-1)^-, t) = \beta \frac{\partial T}{\partial x}((n-1)^+, t), \quad 0 \le \beta \le 1. \tag{4.1}$$

Here β is the *heat retention coefficient*, which is one in the case of continuity of flux, which we assumed previously. For $\beta < 1$, the 'missing' heat can be thought of as leaking out through the portion of the lower surface of the layer not in contact with the substrate. Naturally, T is assumed to be continuous at $z = n - 1$.

One may ask why we impose such a condition only at $z = n - 1$, rather than at welds deeper in the substrate. From an experimental perspective, we note that the discrepancy in the fit holds only for short times. Therefore, we expect that any errors from adding the new hot layer would swamp those percolating upward from the substrate (which would presumably take longer to propagate). From a physical perspective, we know that as time passes, the contact area for any particular weld should increase. This is a result of the temperature causing the weld to 'heal', as well as the increased pressure resulting from the placement of additional layers (Coogan & Kazmer, 2020; Gilmer *et al.*, 2019; Luo *et al.*, 2021). Hence we use the same quasisteady approach as before for the substrate.

4.1 *The steady state*

For notational convenience, we replace (3.3) by

$$T(z,t) = S(z) + \mathrm{e}^{-2\alpha^2 \nu t}\psi(z,t). \tag{4.2}$$

Hence (3.4) and (2.8) hold; satisfying these equations along with continuity of temperature at $z = n-1$, we obtain

$$S_n(z) = s_n(z) + \begin{cases} Bs_>(n-1)s_<(z), & 0 < z < n-1, \\ Bs_<(n-1)s_>(z), & n-1 < z < n, \end{cases} \tag{4.3}$$

$$s_<(z) = \sinh(z\sqrt{2\nu}), \tag{4.4a}$$

$$s_>(z) = \cosh(\sqrt{2\nu}(n-z) + \theta), \tag{4.4b}$$

where B is an as-yet-undetermined constant. For the steady state, (4.1) becomes

$$S'((n-1)^-) = \beta S'((n-1)^+). \tag{4.5}$$

Substituting (4.3) into (4.5) and solving, we have the following:

$$B = \frac{(\beta - 1)s'(n-1)}{J_n(\beta)}, \tag{4.6a}$$

$$J_n(\beta) = s_>(n-1)s'_<(n-1) - \beta s_<(n-1)s'_>(n-1). \tag{4.6b}$$

Note that if $\beta = 1$, $B = 0$ and our results reduce to those in the previous section. To do the computations for the fitting, we need to work through all the details using (3.5) and (4.4a), yielding

$$B = \frac{\beta - 1}{J_n(\beta)} \frac{T_\mathrm{e}\sqrt{2\nu}\sinh(\sqrt{2\nu} + \theta)}{\cosh(n\sqrt{2\nu} + \theta)}, \tag{4.7a}$$

$$J_n(\beta) = \sqrt{2\nu}\left[\cosh(\sqrt{2\nu}+\theta)\cosh((n-1)\sqrt{2\nu}) + \beta\sinh((n-1)\sqrt{2\nu})\sinh(\sqrt{2\nu}+\theta)\right]. \quad (4.7b)$$

4.2 *The transient solution*

The same adjustment process has to be used for the eigenfunctions. In particular, the system (2.14), (2.15) now has to be augmented by

$$u'((n-1)^-) = \beta u'((n-1)^+), \quad (4.8)$$

with continuity of u at $z = n-1$. Solving (2.14) subject to (2.15a) and continuity at $z = n-1$, we obtain

$$u(z) = \begin{cases} \sin\lambda z \sin\lambda(n-1-\phi), & 0 < z < n-1, \\ \sin\lambda(n-1)\sin\lambda(z-\phi), & n-1 < z < n, \end{cases} \quad (4.9)$$

where ϕ is a constant shift factor. Substituting (4.9) into (2.15b) yields

$$\lambda\cos\lambda(n-\phi) = -\nu\sin\lambda(n-\phi), \quad (4.10a)$$

which defines ϕ for any λ. Similarly, substituting (4.9) into (4.8), we have the following:

$$\tan\lambda(n-1-\phi) = \beta\tan\lambda(n-1). \quad (4.10b)$$

Equations (4.10) close the system. As expected, if $\beta = 1$, equation (4.10b) says that ϕ must be 0, in which case the solution reduces to (2.16).

Now that (2.17) is replaced by

$$\psi(z,\tau) = \sum_{m=1}^{\infty} c_m \exp\left(-\alpha^2\lambda_m^2\tau\right) u_m(z), \quad (4.11)$$

the solution is complete once the c_m has been determined. Unfortunately, though the operator in (2.14) is formally self-adjoint, the addition of the condition (4.8) means the underlying eigenvalue problem is not.

To see this, we proceed in the usual way by taking the inner product of u_m'' with v_j, another function that satisfies (2.14) with eigenvalue μ_j. Working out the integration by parts, we have

$$\int_0^n u_m'' v_j \,\mathrm{d}z = [u_m' v_j - u_m v_j']_0^{n-1} + [u_m' v_j - u_m v_j']_{n-1}^n + \int_0^n u_m v_j'' \,\mathrm{d}z.$$

Here the bracketed terms (the *bilinear concomitant*) must vanish. Requiring that v_m also satisfies (2.15) takes care of the boundary terms, in which case the above equation reduces to

$$-\lambda_m^2 \int_0^n u_m v_j \,\mathrm{d}z = -[u_m' v_j - u_m v_j']_{(n-1)^-}^{(n-1)^+} - \mu_j^2 \int_0^n u_m v_j \,\mathrm{d}z,$$

where we have used (2.14). This form makes it clearer that once the bracketed terms have been made to vanish, u_m and v_j will be orthogonal for $j \neq m$.

Using continuity of u and (4.8) in the above equation, we see that in order for the bilinear concomitant to vanish, the following conditions must hold:

$$v(n-1)^+ = \beta v(n-1)^-, \qquad v'(n-1)^+ = v'(n-1)^-. \tag{4.12}$$

Hence for the adjoint problem, in contrast to u, v' is continuous at $z = n-1$, and it is v that has a jump. (In the case that $\beta = 1$, these are just continuity conditions and the problem becomes self-adjoint.)

Solving (2.14) subject to (2.15a) and the continuity condition in (4.12), we have

$$v(z) = \begin{cases} \sin \lambda z \cos \lambda(n-1-\phi), & 0 < z < n-1, \\ \cos \lambda(n-1) \sin \lambda(z-\phi), & n-1 < z < n. \end{cases} \tag{4.13}$$

Substituting (4.13) into (2.15b) and the jump condition in (4.12) yields (4.10), as expected. Hence the adjoint problem has the same eigenvalues.

Since the problem is not self-adjoint, the coefficients c_m are calculated by taking the inner product of $\psi(z,0)$ with the *adjoint* functions v_m, and then normalizing by the inner product of u_m and v_m. Hence (3.7a) is replaced by the expression

$$\begin{aligned} \langle u_m, v_m \rangle c_m &= \int_0^{n-1} [S_{n-1}(z) - S_n(z)] v_m(z)\, \mathrm{d}z + \int_{n-1}^{n} [1 - S_n(z)] v_m(z)\, \mathrm{d}z \\ &= M(n-1) - M(n) + \int_{n-1}^{n} v_m(z)\, \mathrm{d}z, \end{aligned} \tag{4.14a}$$

$$M(y) = \int_0^y S_y(z) v_m(z)\, \mathrm{d}z, \tag{4.14b}$$

in a somewhat analogous notation to (3.9). The first term simplifies greatly due to the boundary conditions imposed at $z = n$:

$$M(n) = \frac{\nu T_\mathrm{e}}{2\nu + \lambda^2} \left[v_m(n) + 2 \int_0^n v_m(z)\, \mathrm{d}z \right]. \tag{4.15a}$$

In contrast, after much tedious algebra, the other term is found to be

$$\begin{aligned} M(n-1) = &- \frac{(1-\beta) v_m(n-2)}{2\nu + \lambda^2} \frac{s'_{n-1}(n-2) J_{n-1}(1)}{J_{n-1}(\beta)} + \frac{2\nu T_\mathrm{e}}{2\nu + \lambda^2} \int_0^{n-1} v_m(z)\, \mathrm{d}z \\ &- \left\{ \frac{S_{n-1} v'_m + [\nu(S_{n-1} - T_\mathrm{e})] v_m}{2\nu + \lambda^2} \right\}_{z=(n-1)^-}. \end{aligned} \tag{4.15b}$$

If we define the right-hand side of (4.14a) as R, then combining (4.15) and computing the integral, we obtain

$$R = \left(1 - \frac{2\nu T_e}{2\nu + \lambda^2}\right) \frac{v_m'((n-1)^+}{\lambda^2} - \left\{ \frac{S_{n-1}v_m' + [\nu(S_{n-1} - T_e)]v_m}{2\nu + \lambda^2} \right\}_{z=(n-1)^-} + \frac{\nu(1 - T_e)v_m(n)}{\lambda^2} - \frac{(1-\beta)v_m(n-2)s_{n-1}'(n-2)J_{n-1}(1)}{(2\nu + \lambda^2)J_{n-1}(\beta)},$$

which may be simplified using (3.5) and (4.7b) to obtain

$$R = \left(1 - \frac{2\nu T_e}{2\nu + \lambda^2}\right) \frac{v_m'((n-1)^+}{\lambda^2} - \left\{ \frac{S_{n-1}v_m' + [\nu(S_{n-1} - T_e)]v_m}{2\nu + \lambda^2} \right\}_{z=(n-1)^-} + \frac{\nu(1 - T_e)v_m(n)}{\lambda^2} - \frac{2\nu(1-\beta)T_e v_m(n-2)\sinh(\sqrt{2\nu} + \theta)}{(2\nu + \lambda^2)J_{n-1}(\beta)}. \tag{4.16}$$

The computation of c_m can then be completed using (4.3), (4.7b), (4.13), and the normalization factor, which is given by

$$\langle u_m, v_m \rangle = \frac{(n-1)\sin(2\lambda_m(n-1-\phi_m))}{4} + \frac{\sin(2\lambda_m(n-1))}{4}\left[1 - \frac{\sin 2\lambda_m(n-\phi_m)}{2\lambda_m}\right]. \tag{4.17}$$

The system (4.10) must be solved numerically, and has multiple solutions. From a computational perspective, to ensure we did not miss any roots in Matlab, we used both the `fsolve` and `fmincon` algorithms (due to deficiencies in each).

From a theoretical perspective, if (λ, ϕ) is a solution, so is $(\lambda, \phi + j\pi/\lambda)$ because of the periodicity of the tangent. If j is an even integer, all of our expressions are the same. If j is an odd integer, $(u_m, v_m) \mapsto -(u_m, v_m)$. Hence the normalization factor is unchanged, but $R \mapsto -R$, which means that $c_m \mapsto -c_m$. Thus $c_m u_m$ is of the same sign, as expected.

4.3 *Data fitting*

To fit the experimental data, we again calculate the weld temperatures. Because the functions in this section are defined piecewise, some of these are more complicated. For W_2, since both measurements occur for $z < n-1$, $u_m(z)$ is given by the top line in (4.9). Thus we may use (3.10b) with s_n replaced by S_n, and the extra coefficient that distinguishes the top line of (4.9) from the expression in (2.16):

$$W_2(\tau) = \frac{S_n(n-3/2) + S_n(n-5/2)}{2} + \mathrm{e}^{-2\alpha^2\nu t}\sum_{m=1}^{\infty} c_m \exp\left(-\alpha^2\lambda_m^2\tau\right)\sin\lambda_m(n-2)\cos\frac{\lambda_m}{2}\sin\lambda_m(n-1-\phi_m). \tag{4.18a}$$

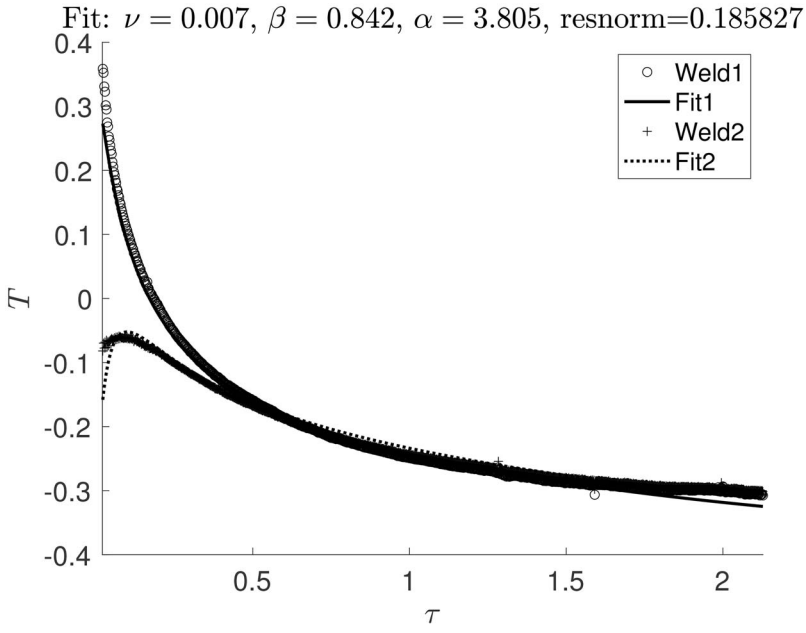

FIG. 6. Plot of two-weld, three-parameter fit of (4.18).

For W_1, since the measurements occur on either side of $z = n - 1$, we revert to (2.22a) and use (4.2), (4.9) and (4.11):

$$W_1(\tau) = \frac{S_n(n-1/2) + S_n(n-3/2)}{2} + \mathrm{e}^{-2\alpha^2\nu t} \sum_{m=1}^{\infty} \frac{c_m \exp\left(-\alpha^2\lambda_m^2\tau\right)}{2} \times \left[\sin\lambda_m\left(n - \frac{1}{2} - \phi_m\right)\sin\lambda_m(n-1) + \sin\lambda_m\left(n - \frac{3}{2}\right)\sin\lambda_m(n - 1 - \phi_m)\right], \quad (4.18b)$$

where we have used (4.9).

We illustrate the data fitting in Fig. 6. In contrast to Fig. 4, the solution for the second weld has the peak at the proper magnitude and the correct place. The values for ν and α are comparable to those found in §3, which indicates that introducing the jump condition merely complements the previous model, rather than introducing large deviations. We also note that the value of β is close to 1, which indicates that though there is some heat loss at the weld, it is not large. Hence the layer and substrate are in near-complete contact, which is more consistent with more sophisticated models of the layer shape (Coogan & Kazmer, 2020; Luo *et al.*, 2021).

4.4 *Parameter dependence*

Recall from (2.4a) that an experimentalist can adjust the value of α by changing t_1 for a particular run. Hence it is important to have an estimate for the sensitivity of our solution to parameters that might change (D'Amico & Peterson, 2020).

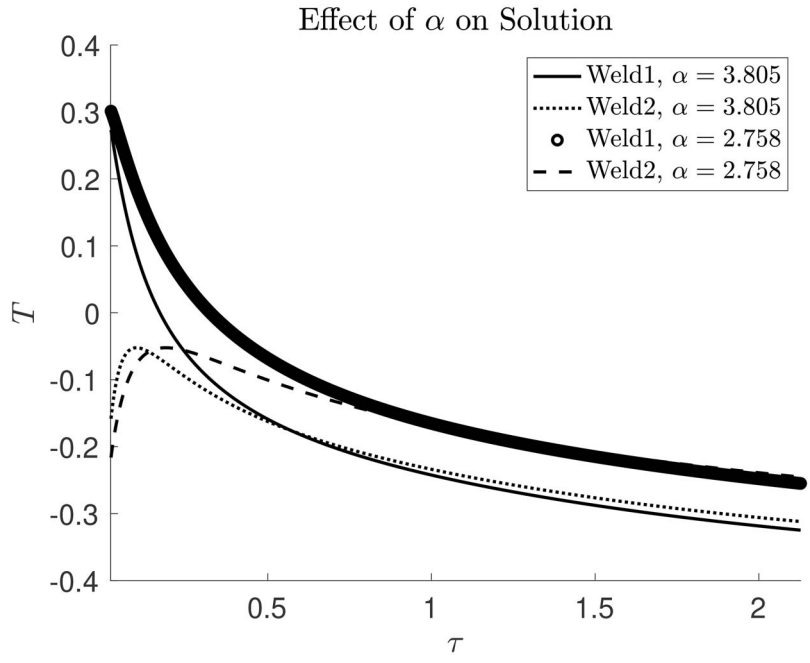

FIG. 7. Variance of computed solution with α. Other parameters are as in Fig. 6.

TABLE 1 *Parameter sensitivity*

Parameter ratio	**Resnorm/Resnorm$_{\text{fit}}$**
$\alpha/\alpha_{\text{fit}} = 0.724$	51.04
$\nu/\nu_{\text{fit}} = 0.689$	73.15
$\nu/\nu_{\text{fit}} = 6.895$	3143.9

In Fig. 7, we show how changing the value of α affects the weld temperature. Recall that since time is always normalized by t_1, the correct interpretation of α is the ratio of the printing time to the diffusion time. As that decreases, we see both a slower rate of cooling, and higher temperatures throughout most of the print time.

There is another reason why we concern ourselves with parameter dependence. As indicated in the Appendix, a range of parameter values for c_p and h appear in the literature, which translates into a possible range of values for ν and α. To determine the sensitivity of our results to these parameters, we performed the following test. Keeping the other two parameters fixed at their value in Fig. 6, we varied the remaining parameter to the extremes of their ranges in Table A2.

The results are shown in Table 1, which shows how the new resnorm compares to the fit value. (Only one comparison with α is shown since the fit value lies slightly above the parameter range shown in the Appendix.) We see that the results have a similar sensitivity to both ν and α, and that the sensitivity is quite strong.

However, we note from Fig. 3 that the dependences can offset one another, as using a low value of one parameter and a high value of another gives a relatively good fit. This behaviour counsels caution

when relying upon just one-parameter fits, as opposed to fitting all parameters where one is unsure of the appropriate value. (The fit values, of course, must be compared with ranges in the literature.)

5. Conclusions and further research

Over the past several years, items created with additive manufacturing are being used in a wider variety of applications (Gibson *et al.*, 2009). As a result, increasing the strength of such items is becoming more important. Items created through FFF are particularly prone to delamination (Coasey *et al.*, 2020); hence an important way to reinforce such items is to strengthen the weld between layers. Due to molecular interactions at layer interfaces, welds are strengthened at increased temperatures (Coogan & Kazmer, 2020; Sun *et al.*, 2008; Turner *et al.*, 2014). As the weld temperature is difficult to measure experimentally, mathematical models can provide needed insight into the strength of such bonds.

In this work we presented three one-dimensional mathematical models of increasing complexity for heat transfer in an object created through FFF. Each is amenable to analytic solution, which makes the interpretation of the results straightforward, as well as understanding the parameter dependence of those solutions. A key assumption made throughout this manuscript is that, given the delay between the placing of layers, the substrate temperature reaches a steady state before the next layer is placed. This allows the computation of the transient Fourier modes to be relatively straightforward.

In the first attempt, we adapted a previously used model (Coasey *et al.*, 2020) which involves solving the one-dimensional heat equation in a domain which expands as additional layers are placed. Unfortunately, this basic model assumes that the entire stack is insulated, except for the top of the applied layer. As such, it overestimates the temperature deep in the substrate, causing poor results (see Fig. 3). There is a significant gap in the weld temperatures that does not occur in the data. In addition, the fit parameter ν is several order of magnitudes larger than one would expect (as a result of heat being dissipated through a very small fraction of the exposed surface).

These defects led us to propose a more realistic quasisteady fin model. We adapted the standard fin model (which is typically used for steady-state computations) for use in our system, which is naturally unsteady due to the addition of more layers. The fin model incorporates heat loss throughout the entire height of the substrate. Though the steady state for this model is somewhat more complicated, the transients change only through the addition of a decay term.

The results shown in Fig. 4 indicate improved performance. The two weld temperatures are much closer together, mimicking the experimental data. The value of ν is much smaller (reflecting the larger surface from which heat loss occurs), in line with values from the literature (see the Appendix). In addition, the value of α, which is also fit, is close to values found in the literature.

However, Fig. 4 also illustrates a shortcoming: an overshoot in the second weld temperature for small times. The previous models assumed that the welds encompassed the entire width of the layer; this was a result of assuming that the layers had a square cross section. In reality, the cross sections have a capsule-like shape (Behdani *et al.*, 2020; Coogan & Kazmer, 2020; Gilmer *et al.*, 2019; Luo *et al.*, 2021), which means that the welds do not span the entire width of the layer.

To model this, in our third attempt we imposed the condition (4.1) at the top weld. Essentially, we assumed that some heat at the weld was being lost to the outside air due to the geometry (see Fig. 5). With this jump condition imposed, the resulting eigenvalue problem in the z-direction was no longer self-adjoint. The eigenfunctions for the adjoint problem were closely related, and we were able to construct (complicated) expressions for the underlying mode coefficients, which could then be converted to weld temperatures.

The results shown in Fig. 6 illustrate even better results. The unphysical peak is now gone, and both simulations closely match their respective welds. The values of ν and α are very close to the previous continuous model, indicating that the addition of the jump does not fundamentally affect most of the solution. And the fact that β remains near 1 shows that this is not a dominant effect (as it affects the fit only for a short time).

Naturally, an even more realistic model would take into account the fact that the individual layers do not have a rectangular cross section (Bellehumeur *et al.*, 2004; Gilmer *et al.*, 2019; Luo *et al.*, 2021). In particular, one can adapt the fin model to the case where the cross section varies with height (Lienhard & Lienhard, 2019, §4.5). Given the complicated nature of the outer boundary of the stack (somewhat cylcloidal in nature; Coogan & Kazmer (2020); Percoco *et al.* (2021)), a numerical simulation would be appropriate. This is the topic of future research.

Though we have drawn a qualitative relationship between the weld temperature and the bond strength, this can be quantified through the introduction of the *healing parameter* (Coogan & Kazmer, 2020; Gilmer *et al.*, 2021; Thomas & Rodríguez, 2000), which relates the temperature history of the weld to bond strength. Incorporating this factor is also the subject of ongoing research.

The results in this work indicate that a well-crafted one-dimensional model can produce analytical results that match experimental data, obviating the need for more computationally intensive numerical simulations. Hence this model should have predictive value in estimating the weld strengths in a wide variety of FFF applications.

Acknowledgements

The author thanks Michael Mackay and Keith Coasey of the University of Delaware for helpful discussions. The author thanks Jonathan Seppala of NIST for helpful discussions, and for providing the raw data for fitting. The author also thanks the reviewer for helpful suggestions which improved the final manuscript.

References

Arslan-Yildiz, A., El Assal, R., Chen, P., Guven, S., Inci, F. & Demirci, U. (2016) Towards artificial tissue models: past, present, and future of 3D bioprinting. *Biofabrication*, **8**, 014103.

Baeza-Campuzaño, A. & Castano, V. M. (2021) The effect of printing velocity on the temperature and viscosity of the polymer thread at the nozzle exit in 3D printers. *Polimery*, **66**, 127–138.

Behdani, B., Senter, M., Mason, L., Leu, M. & Park, J. (2020) Numerical study on the temperature-dependent viscosity effect on the strand shape in extrusion-based additive manufacturing. *Journal of Manufacturing and Materials Processing*, **4**.

Bellehumeur, C., Li, L., Sun, Q. & Gu, P. (2004) Modeling of bond formation between polymer filaments in the fused deposition modeling process. *Journal of Manufacturing Processes*, **6**, 170–178.

Bird, R. B., Stewart, W. E. & Lightfoot, E. N. (1960) *Transport Phenomena*. New York: Wiley.

Coasey, K., Hart, K. R., Wetzel, E., Edwards, D. & Mackay, M. E. (2020) Nonisothermal welding in fused filament fabrication. *Addit. Manuf.*, **33**, 101140.

Coogan, T. J. & Kazmer, D. O. (2020) Prediction of interlayer strength in material extrusion additive manufacturing. *Addit. Manuf.*, **35**, 101368.

Costa, S., Duarte, F. & Covas, J. (2015) Thermal conditions affecting heat transfer in FDM/FFE: a contribution towards the numerical modelling of the process. *Virtual and Physical Prototyping*, **10**, 35–46.

D'Amico, T. & Peterson, A. M. (2020) Bead parameterization of desktop and room-scale material extrusion additive manufacturing: how print speed and thermal properties affect heat transfer. *Addit. Manuf.*, **34**, 101239.

Das, A., McIlroy, C. & Bortner, M. J. (2021) Advances in modeling transport phenomena in material-extrusion additive manufacturing: coupling momentum, heat, and mass transfer. *Progress in Additive Manufacturing*, **6**, 3–17.

Davis, C. S., Hillgartner, K. E., Han, S. H. & Seppala, J. E. (2017) Mechanical strength of welding zones produced by polymer extrusion additive manufacturing. *Addit. Manuf.*, **16**, 162–166.

Edwards, D. A. & Mackay, M. E. (2020) Postextrusion heating in three-dimensional printing. *J. Heat Transfer*, **142**, 052101.

Edwards, D. A., Mackay, M. E., Swain, Z. R., Banbury, C. R. & Phan, D. D. (2019) Maximal 3D printing extrusion rates. *IMA J. Appl. Math.*, **84**, 1022–1043.

Gibson, I., Rosen, D. W. & Stucker, B. (2009) *Additive Manufacturing Technologies: Rapid Prototyping to Direct Digital Manufacturing*, 1st edn. Incorporated: Springer Publishing Company.

Gilmer, E. L., Anderegg, D., Gardner, J. M., Sauti, G., Siochi, E. J., McKnight, S. H., Dillard, D. A., McIlroy, C. & Bortner, M. J. (2021) Temperature, diffusion, and stress modeling in filament extrusion additive manufacturing of polyetherimide: an examination of the influence of processing parameters and importance of modeling assumptions. *Addit. Manuf.*, **48**, 102412.

Gilmer, E. L., Mansfield, C., Gardner, J. M., Siochi, E. J., Baird, D. G. & Bortner, M. J. (2019) *Characterization and Analysis of Polyetherimide: Realizing Practical Challenges of Modeling the Extrusion-Based Additive Manufacturing Process*, chapter 5. ACS Publications, pp. 69–84.

Hager, I., Golonka, A. & Putanowicz, R. (2016) 3D printing of buildings and building components as the future of sustainable construction? *Procedia Engineering*, **151**, 292–299.

Kosky, P., Balmer, R., Keat, W. & Wise, G. (2021) *Exploring Engineering*, 5th edn. Academic Press.

Lechner, M. D. (2018) Polymers. *Springer Handbook of Materials Data* (H. Warlimont & W. Martienssen eds). Springer International Publishing, pp. 489–540.

Lienhard IV, J. H. & Lienhard V, J. J. (2019) *V. A Heat Transfer Textbook*, 5th edn. Mineola, NY: Dover Publications.

Lotero, F., Couenne, F., Maschke, B. & Sbarbaro, D. (2017) Distributed parameter bi-zone model with moving interface of an extrusion process and experimental validation. *Math. Comput. Model. Dyn. Syst.*, **23**, 504–522.

Luo, C., Mrinal, M., Wang, X. & Hong, Y. (2021) Bonding widths of deposited polymer strands in additive manufacturing. *Dent. Mater.*, **14**, 871.

Luo, C., Wang, X., Migler, K. B. & Seppala, J. E. (2020) Upper bound of feed rates in thermoplastic material extrusion additive manufacturing. *Addit. Manuf.*, **32**, 101019.

Mu, Y., Zhao, G., Wu, X., Hang, L. & Chu, H. (2015) Continuous modeling and simulation of flow-swell-crystallization behaviors of viscoelastic polymer melts in the hollow profile extrusion process. *App. Math. Model.*, **39**, 1352–1368.

Najmon, J. C., Raeisi, S. & Tovar, A. (2019) Review of additive manufacturing technologies and applications in the aerospace industry. *Additive Manufacturing for the Aerospace Industry* (F. Froes & R. Boyer eds). Elsevier, pp. 7–31.

Nath, P., Olson, J. D., Mahadevan, S. & Lee, Y.-T. T. (2020) Optimization of fused filament fabrication process parameters under uncertainty to maximize part geometry accuracy. *Addit. Manuf.*, **35**, 101331.

Percoco, G., Arleo, L., Stano, G. & Bottiglione, F. (2021) Analytical model to predict the extrusion force as a function of the layer height, in extrusion based 3D printing. *Addit. Manuf.*, **38**, 101791.

Phan, D. D., Swain, Z. R. & Mackay, M. E. (2018) Rheological and heat transfer effects in fused filament fabrication. *Journal of Rheology*, **62**, 1097–1107.

Rashid, A. A. & Koç, M. (2021) Fused filament fabrication process: a review of numerical simulation techniques. *Polymers*, **13**, 3534.

Seppala, J. E. (Sept. 2020) *Private communication*.

Seppala, J. E., Hoon Han, S., Hillgartner, K. E., Davis, C. S. & Migler, K. B. (2017) Weld formation during material extrusion additive manufacturing. *Soft Matter*, **13**, 6761–6769.

Seppala, J. E. & Migler, K. D. (2016) Infrared thermography of welding zones produced by polymer extrusion additive manufacturing. *Addit. Manuf.*, **12**, 71–76.

Sitison, J. W. & Edwards, D. A. (2020) The heat balance integral method for cylindrical extruders. *J. Engrg. Math.*, **122**, 1–16.

Sun, Q., Rizvi, G. M., Bellehumeur, C. T. & Gu, P. (2008) Effect of processing conditions on the bonding quality of FDM polymer filaments. *Rapid Prototyping Journal*, **14**, 72–80.

Thomas J. & Rodríguez J.. Modeling the fracture strength between fused-deposition extruded roads 16. *2000 International solid freeform fabrication symposium*.

Turner, B. N., Strong, R. & Gold, S. A. (2014) A review of melt extrusion additive manufacturing processes: I. process design and modeling. *Rapid Prototyping Journal*, **20**, 192–204.

van Noort, R. (2012) The future of dental devices is digital. *Dent. Mater.*, **28**, 3–12.

Wu, P., Wang, J. & Wang, X. (2016) A critical review of the use of 3D printing in the construction industry. *Automation in Construction*, **68**, 21–31.

Xia, H., Lu, J., Dabiri, S. & Tryggvason, G. (2018) Fully resolved numerical simulations of fused deposition modeling. Part I: fluid flow. *Rapid Prototyping Journal*, **24**, 463–476.

Yang, F. & Pitchumani, R. (2002) Healing of thermoplastic polymers at an interface under nonisothermal conditions. *Macromolecules*, **35**, 3213–3224.

Appendix

In Table A1, we summarize the relevant parameters from the literature used in this manuscript, while in Table A2 we calculate the parameters of interest to our model; some remarks are noted below.

Recall that $\tilde{T}_\mathrm{h}$ is the temperature of the polymer when first applied. Therefore, we do not use the heater temperature of 210°C given in Seppala *et al.* (2017), as there is always cooling after extrusion (Edwards & Mackay, 2020). Instead, we use the initial condition of the experimental data.

As discussed above, the layers are laid down in sequence. To compute the time t_l between layers, one must add the printing time for a layer to a delay where the printer resets and moves to the initial printing position. As discussed in Seppala *et al.* (2017), the print length is 160 mm and the print speed is 100 mm (this value from the text is correct; the value listed in the caption to Fig. 2 is not (Seppala, Sept., 2020)). The delay is 5.45 s (Seppala, Sept., 2020), which yields

$$t_\mathrm{l} = 5.45\ \mathrm{s} + \frac{160\ \mathrm{mm}}{100\ \mathrm{mm/s}} = 7.05\ \mathrm{s},$$

as indicated in Table A2.

Table A1 *Parameters from the literature*

	Value	Reference
c_p [J/(kg·K)]	1300–2100	Coasey *et al.* (2020); Lechner (2018)
h [W/(m^2·K)]	2.5–25	Kosky *et al.* (2021)
k [W/(m·K)]	0.21	Coasey *et al.* (2020)
L (mm)	0.3	Seppala *et al.* (2017)
$\tilde{T}_\mathrm{e}$ (° C)	23	
$\tilde{T}_\mathrm{h}$ (° C)	194.6	Seppala *et al.* (2017)
$\tilde{T}_\mathrm{p}$ (° C)	110	Seppala *et al.* (2017)
ρ (kg/m^3)	1030	Coasey *et al.* (2020)

TABLE A2 *Calculated parameters*

	Value		Value
T_e	−1.028	ΔT (° C)	84.6
t_l (s)	7.05	ν	4.69×10^{-3}–4.69×10^{-2}
α	2.758–3.505		

Nomenclature

Units are listed in terms of length (L), mass (M), time (T) and temperature (θ). If a symbol appears both with and without tildes, the symbol with tildes has units, while the one without is dimensionless. Equation numbers where a variable is first defined is listed, if appropriate.

A: area of transverse cross section, units L^2.

B: constant in second fin model (4.3).

c: coefficient in eigenfunction expansion (2.17).

c_p: heat capacity of polymer, units $L^2/(T^2\theta)$ (2.1).

$F(\tau)$: separation-of-variables component (2.13).

$H(\cdot)$: integration result for basic model (2.20).

h: heat transfer coefficient, units $L/(T^3\theta)$.

$J(\beta)$: intermediate calculation (4.6b).

j: integer, variously defined.

$K(\cdot)$: integration result for first fin model (3.8).

k: thermal conductivity, units $ML/(T^3\theta)$ (2.1).

L: layer height, units L.

$M(\cdot)$: integration result for second fin model (4.14b).

m: mode index (2.17).

n: number of layers (2.5).

P: perimeter of transverse cross section, units L.

R: intermediate result (4.16).

$S(z)$: steady state solution of second fin model (4.2).

$s(z)$: steady state solution of first fin model (3.3).

$\tilde{T}$: temperature, units θ (2.1).

$\tilde{t}$: time, units T (2.1).

$u(z)$: eigenfunction (2.14).

$v(z)$: eigenfunction of adjoint problem.

$W(\tau)$: weld temperature (2.22).

w: length of layer, units L (3.1).

y: dummy limit of integration (2.20).

$\tilde{z}$: height along stack, units L (2.1).

ΔT: differential between heater and plate temperatures, units θ (2.3).

α: square root of thermal diffusivity (2.4a).

β: heat retention coefficient (4.1).

θ: phase shift in steady state (3.5).

λ: eigenvalue in separation-of-variables expansion (2.13).

μ: eigenvalue of adjoint problem.

ν: dimensionless heat transfer coefficient (2.5).

ρ: density of polymer, units M/L^3 (2.1).

$\sigma(z)$: steady state solution of basic model (2.7).

τ: shifted time scale (2.9).

ϕ: phase shift in eigenfunction (4.9).

$\psi(z,\tau)$: transient solution (2.10).

Other notation

e: as a subscript on T, used to indicate the external temperature (2.5).

h: as a subscript on T, used to indicate temperature of the applied layer (2.3).

l: as a subscript on t, used to indicate the interval between layer applications (2.3).

n: as a subscript, used to indicate layer number (2.7).

p: as a subscript on T, used to indicate temperature of the build plate (2.2).

$>$: as a subscript on s, used to indicate above the first weld (4.3).

$<$: as a subscript on s, used to indicate below the first weld (4.3).